Using the stochastic-threshold incision model to understand the tectonic expression on fluvial topography: theory and application to the Dadu River basin, eastern Tibetan Plateau

Yizhou Wang[1], Dewen Zheng[1], Huiping Zhang[2], Taylor Schildgen[3], Fiona Clubb[4], Matthew Fox[5], and Eitan Shelef[6]

[1]Institute of Geology, China Earthquake Administration
[2]State Key Laboratory of Earthquake Dynamics, Institute of Geology, China Earthquake Administration
[3]GFZ Potsdam
[4]Durham University
[5]University College London
[6]University of Pittsburgh

December 8, 2022

Abstract

The non-linear reliance of channel steepness on erosion rates can be reconciled by the stochastic-threshold incision model that incorporates river incision threshold and discharge probability distribution into erosion efficiency. Here, we explored the usage of the model in river longitudinal profile inversion, by assuming time-dependent tectonic forcing and a linear exponent that relates channel incision to slope. We developed an analytical solution to the model equation and an inverse scheme to retrieve relative uplift rate history, whose validity was based on the theoretical demonstration on knickpoint preservation. Application of the inverse scheme to the main trunks of the Dadu River basin in the eastern Tibetan Plateau produced a history with two-phase increases in the uplift/incision rates, which is similar to the results from low-temperature thermochronology. Thus, our analytical procedures provide new insights into the link of tectonic uplift and river profile evolution, when channel steepness depends on erosion rates non-linearly.

Hosted file

951448_0_art_file_10513453_rmc082.docx available at https://authorea.com/users/552132/articles/611244-using-the-stochastic-threshold-incision-model-to-understand-the-tectonic-expression-on-fluvial-topography-theory-and-application-to-the-dadu-river-basin-eastern-tibetan-plateau

Using the stochastic-threshold incision model to understand the tectonic expression on fluvial topography: theory and application to the Dadu River basin, eastern Tibetan Plateau

Yizhou Wang, Dewen Zheng, and Huiping Zhang

State Key Laboratory of Earthquake Dynamics, Institute of Geology, China Earthquake Administration, Beijing 100029, China

Corresponding author: Yizhou Wang (wangyizhou2016@outlook.com)

Key Points:

- Assuming timely dependent tectonic uplift, we present an analytic solution to the linear stochastic-threshold incision model equation.

- The analytic solution yields a linear inverse scheme to decipher tectonic uplift rate history from river longitudinal profiles.

- Two-phase increase in the uplift/incision rates that initiated at the late Miocene and early Pleistocene was inferred for the Dadu basin.

Abstract

The non-linear reliance of channel steepness on erosion rates can be reconciled by the stochastic-threshold incision model that incorporates river incision threshold and discharge probability distribution into erosion efficiency. Here, we explored the usage of the model in river longitudinal profile inversion, by assuming time-dependent tectonic forcing and a linear exponent that relates channel incision to slope. We developed an analytical solution to the model equation and an inverse scheme to retrieve relative uplift rate history, whose validity was based on the theoretical demonstration on knickpoint preservation. Application of the inverse scheme to the main trunks of the Dadu River basin in the eastern Tibetan Plateau produced a history with two-phase increases in the uplift/incision rates, which is similar to the results from low-temperature thermochronology. Thus, our analytical procedures provide new insights into the link of tectonic uplift and river profile evolution, when channel steepness depends on erosion rates non-linearly.

Keywords: stochastic-threshold incision model, time-dependent tectonic uplift, linear slope exponent, analytical solution, inverse scheme

Plain Language Summary

River incision into channel bedrock occurs only when the stream power generated by large floods overcomes the critical value of shear stress. Despite the assumption of a linear dependency of river erosion on channel gradients, the linear stochastic-threshold incision model that incorporates both incision threshold and runoff variability can predict the monotonic, non-linear increase of channel steepness with erosion rates. Channel steepness measures the slope normalized for drainage area. Considering time-dependent tectonic uplift, we presented an analytical solution to the linear stochastic-threshold model equation and derived an inversion scheme to decode the temporary changes in the relative uplift rates from river long profiles. The inverse scheme was successfully applied to the Dadu River that flows through the eastern margin of the Tibetan Plateau. Our analytical work thus helps to decipher the expression of active tectonics in erosional landscapes.

1 Introduction

In active mountain ranges, the fluvial system evolves as a response to the spatiotemporal changes in both tectonic and climatic forcing [Howard and Kerby, 1983; Whipple and Tucker, 1999]. The fluvial channels adjust their profile shape by modulating the pattern of erosion and sediment transport, exerting a first control on orogen-scale relief [Whipple and Tucker, 2002; Kirby and Whipple, 2012]. Since decades, a great many models have been proposed to link the processes between tectonic uplift, climate change, river incision, and landscape evolution [e.g. Howard and Kerby, 1983; Howard, 1994; Johnson and Whipple, 2007; Lague, 2014]. Instead of relating to the physics of specific incision process, the stream-power incision model (SPIM) presents the channel bedrock incision rate, E [L/T], in terms of channel slope, S [L/L], and upstream drainage area, A [L^2] [Howard and Kerby, 1983]:

$$\frac{\partial z(t,x)}{\partial t} = U(t,x) - E(t,x) = U(t,x) - KA^m \left[\frac{\partial z(t,x)}{\partial x}\right]^n \quad (1)$$

63   where U [L/T] is tectonic uplift rate, z [L] is channel elevation, x [L] is horizontal upstream
64   distance along the channel, $S = \partial z / \partial x$ is channel slope, t [T] is time, and K [L^{1-2m}/T] is channel
65   erodibility coefficient. m and n are positive exponents that measure the significance of drainage
66   area and slope to erosion, respectively.

67   Although numerical solutions to Equation (1) usually have been used in landscape evolution
68   forward models [e.g. Tucker et al., 2001; Refice et al., 2012], inversion on the river long profiles
69   calls for analytical solutions to the SPIM equation [Pritchard et al., 2009; Goren et al., 2014,
70   2021]. Assuming a linear erosion–slope relationship, i.e. $n = 1$, analytical solutions to Equation
71   (1) were derived and the related inversion schemes were developed to infer the climatic and/or
72   tectonic conditions in many active landscapes [Goren et al., 2014; Rudge et al., 2015; Goren,
73   2016]. However, a growing body of evidences, at both the regional and global scales, have
74   shown non-linear relationships between erosion rates and channel steepness that measures
75   channel gradients normalized for downstream increases in drainage area [e.g. Harkins et al.,
76   2007; Harel et al., 2016; Hilley et al., 2019]. These findings thus questions the validity of the
77   routinely used linear assumption ($n = 1$). Combing $n \neq 1$ and timely variable tectonic uplift,
78   analytical solutions to Equation (1) predicts the formation of stretch zones that contains no
79   tectonic information and consuming and merging knickpoints where the tectonic signals could
80   partly and even entirely lost [Royden and Perron, 2013; Wang et al., 2022]. The non-linear
81   dynamics thus hinder formal attempts to relate the channel profile form to tectonic history.

82   Alternatively, many studies have found that the non-linear erosion–steepness scaling does
83   not necessarily require a non-linear slope exponent n [Snyder et al., 2003; Lague et al., 2005;
84   Dibiase and Whipple, 2011]. Rather, even if using $n = 1$, the observed relation of non-linear
85   increase of channel steepness with increasing erosion rate can well be reconciled by taking the
86   effects of both bedrock resistance to erosion and the effectiveness of stream power [Whipple,
87   2009; Scherler et al., 2017]. These studies emphasized that river incision was actually triggered
88   by large floods that generates high stream power to overcome the channel substrate detachment
89   thresholds, which is not presented in the simple SPIM (Equation 1).

90   In this contribution, we followed DiBiase and Whipple [2011] to construct the transient
91   equation of the stochastic-threshold incision model (STIM) that incorporates both the incision
92   threshold and discharge distribution function. Then, by assuming a timely dependent $U(t)$ and
93   linear n, we derived an analytical solution to the STIM equation and presented an inversion
94   scheme to infer $U(t)$ from river long profiles. As a case study, we applied the inverse scheme to
95   the Dadu River basin that drains parts of the eastern Tibetan Plateau.

96

2 A mathematical expression of the stochastic-threshold incision model (STIM)

98   Stream power incision into the detachment-limited channel bed occurs when the bed shear
99   stress, τ [Pa], overcome a critical value (τ_c). The instantaneous vertical incision rate, I, scales
100   with τ in the term of a power-law function [Howard and Kerby, 1983]:

$$I = k_e \cdot (\tau^a - \tau_c^a) \quad (2)$$

102   where k_e quantifies the channel substrate resistance to incision and a depends on specific incision
103   mechanism. Following the assumptions of steady, uniform flow and negligible bank friction
104   [Howard, 1994], Dibiase and Whipple [2011] defined τ as:

105
$$\tau = k_t \cdot \left(\frac{Q}{w}\right)^\alpha \cdot \left(\frac{\partial z}{\partial x}\right)^\beta \quad (3)$$

106 where k_t is a constant that incorporates water density, gravitational and frictional terms, Q [L^3/T]
107 is river discharge, and w [L] is channel width, and α and β are positive exponents. Hydrologic
108 records or field measurements support a power-law to relate bankfull channel width (w_b) to
109 mean-annual discharge ($\bar{Q}$) [Montgomery and Gran, 2001; Zhang et al., 2017]:

110
$$w_b = k_w \bar{Q}^{\omega_b} \quad (4)$$

111 where k_w and ω_b are empirical scaling parameters. To incorporate the stochastic distribution of
112 discharge into bed shear stress (Equation 3), we followed Scherler et al. [2017] to adopt a
113 geometrical treatment that channel width (w) changes as a function of discharge (Q):

114
$$\frac{w}{w_b} = \left(\frac{Q}{\bar{Q}}\right)^{\omega_s} \quad (5)$$

115 where ω_s is also an empirical scaling parameter. Mean-annual discharge ($\bar{Q}$) usually correlates
116 with drainage area [Tucker, 2004]:

117
$$\bar{Q} = R_b A^c \quad (6)$$

118 where c is positive exponent and R_b (L/T) represents mean annual catchment-integrated runoff.
119 Assigning Equations (3-6) into (2), we derived:

120
$$I = k_e k_t^a k_w^{-\alpha a} R_b^{\alpha a(1-\omega_b)} \cdot \left(\frac{Q}{\bar{Q}}\right)^{\alpha a(1-\omega_s)} \cdot A^{\alpha a c(1-\omega_b)} \cdot \left(\frac{\partial z}{\partial x}\right)^{\beta a} - k_e \tau_c^a \quad (7)$$

121   To make Equation (7) concise, we followed Dibiase and Whipple [2011] to define four
122 variables, $\kappa = k_e k_t^a k_w^{-\alpha a} R_b^{\alpha a(1-\omega_b)}$, $\gamma = \alpha a(1-\omega_s)$, $\Psi = k_e \tau_c^a$, and $Q^* = \frac{Q}{\bar{Q}}$. Q^* is normalized
123 discharge. In the simple form of the SPIM (Equation 1), $m = \alpha a(1-\omega_b)$ and $n = \beta a$. Thus,
124 Equation (7) can be written as:

125
$$I = \kappa \cdot (Q^*)^\gamma \cdot A^{cm} \cdot \left(\frac{\partial z}{\partial x}\right)^n - \Psi \quad (8)$$

126   The probability density function (PDF) of normalized discharge (Q^*) can be defined as
127 [Lague et al., 2005]:

128
$$\text{PDF}(Q^*) = \frac{k^{k+1}}{\Gamma(k+1)} e^{-k/Q^*} Q^{*-(k+2)} \quad (9)$$

129 where Γ is the gama function, and k is the discharge variability parameter. The long-term erosion
130 rate (E_{s-c}) that incorporates the stochastic distribution of discharge thus can be produced by
131 integrating I over the range of all possible discharges:

132
$$E_{s-c} = \int_{Q_c^*}^{Q_m^*} \left[\kappa \cdot (Q^*)^\gamma \cdot A^{cm} \cdot \left(\frac{\partial z}{\partial x}\right)^n - \Psi\right] \cdot \frac{k^{k+1}}{\Gamma(k+1)} e^{-k/Q^*} Q^{*-(k+2)} dQ^* \quad (10)$$

133 where $Q_m^* = Q_m/\bar{Q}$ and $Q_c^* = Q_c/\bar{Q}$. Q_m is the maximum possible discharge and Q_c is the
134 critical discharge to overcome the threshold shear stress. As long as Q_m is sufficiently large, the
135 integration of Equation (10) is insensitive to the choice of Q_m [Lague et al., 2005]. Equation (10)
136 contains two terms, one of which represents stream power incision (E_s) and another relates to
137 erosion thresholds (E_c):

138
$$E_s = K' \cdot A^{cm} \cdot \left(\frac{\partial z}{\partial x}\right)^n \quad (11)$$

139 $$E_c = \Psi \cdot \frac{k^{k+1}}{\Gamma(k+1)} \cdot \int_{Q_c^*}^{Q_m^*} e^{-k/Q^*} Q^{*-(k+2)} \, dQ^* \quad (12)$$

140 where $K' = \kappa \cdot \frac{k^{k+1}}{\Gamma(k+1)} \cdot \int_{Q_c^*}^{Q_m^*} (Q^*)^{\gamma-(k+2)} \cdot e^{-k/Q^*} dQ^*$ depends on the critical discharge Q_c^*. If

141 assuming $c = 1$ and neglecting the effects of incision threshold (i.e. $E_c = 0$), Equation (10)

142 reduces to the simple form of incision rate (E) in Equation (1). We replaced E with E_{s-c} in

143 Equation (1):

144 $$\frac{\partial z}{\partial t} = U(t,x) - K'(Q_c^*) \cdot A^{cm} \cdot \left(\frac{\partial z}{\partial x}\right)^n + E_c(Q_c^*) \quad (13)$$

145 Equation (13) is the mathematical form of the stochastic-threshold incision model (STIM).

146

3 Analytical description of the STIM equation

148

3.1 An integral approach to the steady-state form of the model equation

150 Assuming a balance between uplift rates and long-term erosion rates, i.e. Equation (13)

151 equals to zero, we derived:

152 $$U(x) = K'(Q_c^*) \cdot A^{cm} \cdot S^n - E_c(Q_c^*) \text{ or } S = A^{-cm/n} \cdot \left[\frac{U(x)+E_c(Q_c^*)}{K'(Q_c^*)}\right]^{1/n} \quad (14)$$

153 If under the spatially uniform uplift pattern, i.e. $U(x) = U$, the incision efficiency and threshold

154 related parameters, also should be constants along the river profile, i.e. $E_c(Q_c^*) = E_c$ and $K'(Q_c^*) =$

155 K'. Thus, Equation (14) reduces to:

156 $$S = A^{-cm/n} \cdot \left(\frac{U+E_c}{K'}\right)^{1/n} \quad (15)$$

157 Equation (15) has the same form of the slope-area scaling for a graded river profile [Howard and

158 Kerby, 1983]. Here, channel concavity $\theta = cm/n$ and steepness $k_s = \left(\frac{U+E_c}{K'}\right)^{1/n}$.

159 Performing the integration in the upstream direction yields an analytical solution to

160 Equation (15):

161 $$z = z_b + \left(\frac{U+E_c}{K'}\right)^{1/n} \cdot \left(\frac{1}{A_0}\right)^{cm/n} \cdot \varphi(x) \quad (16)$$

162 $$\text{with } \varphi(x) = \int_0^x \left[\frac{A_0}{A(x')}\right]^{cm/n} dx' \quad (17)$$

163 where z_b is elevation of the base level and A_0 is a reference drainage area. Accordingly,

164 Equations (16-17) produces a $\varphi - z$ plot, which is similar to the $\chi - z$ plot when $c = 1$ [Perron

165 and Royden, 2013].

166 The steady-state form produces a way to determine the normalized critical discharge Q_c^*.

167 Assigning Equation (15) into (8) and setting $I = 0$ yields [Dibiase and Whipple, 2011]:

168 $$Q_c^* = \left(\frac{\Psi}{\kappa \cdot k_s^n}\right)^{1/\gamma} \quad (18)$$

169

170   **3.2 A closed form analytical solution to the linear transient equation**

171   By adopting $n = 1$ ($a = 3/2$ and $\beta = 2/3$ [Dibiase and Whipple, 2011]) and timely
172   dependent uplift rate $U(t)$, Equation (13) can be re-arranged as:

173   $$\frac{\partial z}{\partial t} + K'(Q_c^*) \cdot A^{cm} \cdot \frac{\partial z}{\partial x} = U(t) + E_c(Q_c^*) \ (19)$$

174   In the transient equation, K' and E_c are the functions of critical discharge that relates to channel
175   steepness. It means that both K' and E_c can vary with $U(t)$. Thus, Equation (19) is difficult to be
176   solved, if focusing on the whole river profile. Instead, we followed Wang et al. [2022] to deal
177   with separate transient knickpoints.

178   The elevation change of a knickpoint that formed as a response to the change in tectonic
179   uplift rates can be expressed as:

180   $$\frac{dz(t,x)}{dt} = \frac{\partial z}{\partial t} + \frac{\partial z}{\partial x} \cdot \frac{dx}{dt} \ (20)$$

181   Compared with Equation (19), we can derive two characteristic equations:

182   $$\frac{dx}{dt} = K'(Q_c^*) \cdot A^{cm} \ (21)$$

183   $$\frac{dz}{dt} = U(t) + E_c(Q_c^*) \ (22)$$

184   Notably, it is unlike the condition of Equation (1) where incision efficiency keeps a constant
185   through both time and space. In that case, all the knickpoints share a common retreat velocity
186   formula and can be well preserved [Berlin and Anderson, 2007]. Here, however, for a specific
187   knickpoint, the parameter $K'(Q_c^*)$ in the retreat velocity term (Equation 21) relates to the uplift
188   rate that generated the knickpoint. This means that river incision efficiency varies through time
189   and space, in terms of a step function. In the $x - z$ domain, it might be difficult to determine
190   whether all the knickpoints are preserved.

191   Assuming knickpoint preservation, Equation (21) can be solved:

192   $$t = \int_0^x \frac{1}{K'(Q_c^*) \cdot A^{cm}} dx + t_s = \frac{1}{A_0^{cm} \cdot K'(Q_c^*)} \int_0^x [\frac{A_0}{A(x\prime)}]^{cm} dx + t_s = \frac{1}{A_0^{cm} \cdot K'(Q_c^*)} \varphi(x) + t_s \ (23)$$

193   where t_s indicates a transient signal formed at the base level when $t = t_s$. This implies a
194   boundary condition of $x = 0$ and $z = 0$ at $t = t_s$ [Goren et al., 2014; Rudge et al., 2015].
195   Equation (23) measures a response time for a knickpoint migration from river outlet to its present
196   location.

197   Equation (22) can be solved:

198   $$z = \int_0^t [U(t') + E_c(Q_c^*)] \, dt' + z_s \ (24)$$

199   where z_s is a constant term that can be derived by using the boundary condition:

200   $$z_s = -\int_0^{t_s} [U(t') + E_c(Q_c^*)] \, dt' \ (25)$$

201   Assigning Equations (23 and 25) into (24), we derived the closed form analytical solution to the
202   linear model:

203   $$z = \int_{t_s}^t [U(t') + E_c(Q_c^*)] \, dt' = \int_{t - \frac{1}{A_0^{cm} \cdot K'(Q_c^*)} \varphi(x)}^t [U(t') + E_c(Q_c^*)] \, dt' \ (26)$$

204 Since K' is usually unknown, a non-dimensional K'-independent uplift history is needed. We
205 followed Goren et al. [2014] to define two new variables:

206
$$t^* = t \cdot A_0^{cm} \cdot K'(Q_c^*) \text{ (27)}$$

207
$$\text{and } U^*(t^*) = [U(t) + E_c(Q_c^*)]/(A_0^{cm} \cdot K'(Q_c^*)) \text{ (28)}$$

208 Thus, Equation (26) can be related to a K'-independent uplift history:

209
$$z(t^*, x) = \int_{t^*-\varphi(x)}^{t^*} U^*(t^{*\prime}) \, dt^{*\prime} \text{ (29)}$$

210 Hence, Equation (29) represents the knickpoint evolution in the $\varphi - z$ domain and segments
211 between knickpoints are straight lines.

212

4 A linear inverse scheme to infer tectonic uplift history

214 The analytical solution provides a linear inverse scheme that takes the river long profiles as
215 input data to infer the relative uplift rate history. According to Equation (29), the present channel
216 profile (at $t = 0$) is:

217
$$z(x) = \int_{-\varphi(x)}^{0} U^*(t^*) \, dt^* \text{ (30)}$$

218 We proposed three steps to infer the uplift history. First, via Equations (16-17), we
219 transformed the river long profiles to $\varphi - z$ plots. A series of cm values were using and the one
220 that minimizes the scatter in the $\varphi - z$ domain was selected [e.g. Goren et al., 2014; Shelef et al.,
221 2018]. Second, we defined knickpoints $[(\varphi_1, z_1), (\varphi_2, z_2), \dots (\varphi_{N-1}, z_{N-1})]$ to divide the $\varphi - z$
222 domain into N segments. The basin outlet is identified with $(\varphi_0 = 0, z_0 = 0)$ and the highest
223 channel head is $(\varphi_N = \varphi_{max}, z_N = z_{max})$. These data points are assumed to share a common
224 uplift history (i.e. spatially uniform uplift pattern). Segment j, between $[(\varphi_{j-1}, z_{j-1}), (\varphi_j, z_j)]$, is
225 characterized by a uniform steepness index that shaped the river profile during time interval
226 (t_{j-1}, t_j), where t_j is the time for a transient signal migrating from the river outlet (x_0 or φ_0) to
227 the point (x_j or φ_j). In this way, we can re-write Equation (30) as:

228
$$z(x_j) = \int_{-\varphi_j}^{0} U^*(t^*) \, dt^* = \sum_{i=1}^{j} U_i^* \cdot (\varphi_i - \varphi_{i-1}) \text{ (31)}$$

229 where φ_j equals to t_j^*. U_j^* can be estimated by a linear regression on the data points within the
230 time interval $(\varphi_{j-1}, \varphi_j)$. Consequently, a non-dimensional uplift history, (U_j^*, t_j^*), without any
231 prior information on K', can be derived. Third, conversion from (U_j^*, t_j^*) to a dimensional history
232 (U_j, t_j) by solving equations (27-28), after K' is independently constrained.

233 The inferred uplift history depends on how to choose the φ interval, which can be evaluated
234 based on the misfit function. Combing the non-dimensional history and Equation (31), we can
235 modelled the channel profiles. We followed Wang et al. [2022] to calculate the elevation misfit
236 between the modelled and actual river profiles:

237
$$\text{misfit} = \frac{1}{M/N} \sqrt{\sum_{i=1}^{M}(z_i - \tilde{z}_i)^2} \text{ (32)}$$

238 where M is the number of pixels in the river profile data. z_i and $\tilde{z}_i$ are the actual and modelled
239 elevation at the channel node i.

240

5 Application: linear inversion on the channel profiles of the Dadu River basin

242 We present an application of the linear inverse scheme to the Dadu River, in the eastern
243 margin of the Tibetan Plateau. The river basin is a transient landscape, characterized by high-
244 elevation, low-relief topography in the interior of the Songpan-Ganze block and steep margins
245 deeply dissected by the major trunk and tributaries of large rivers (Figure 1a). Rock exhumation
246 rates in the region increased dramatically at 9-13 Ma, suggesting synchronous fluvial response to
247 the regional uplift initiated at that time [Clark et al., 2005; Tian et al., 2015]. Another event of
248 the Dadu-Anning capture was dated at the early Pleistocene that the upstream of the paleo
249 Anning River was captured by the trunk of the present Dadu River at Shimian and then flowed
250 into the Sichuan Basin [Clark et al., 2004; Yang et al., 2019; Wang et al., 2021].

251 We selected five long main trunks distributed in the Dadu River basin (Figure 1a), which
252 was chosen as a case study in Wang et al. [2022]. We extracted the long profiles of these rivers
253 and observed two generations of knickpoints at the elevations of about 1700 and 3000-3500 m
254 (Figure 1b). Adopting $c = 1$ and $m = 0.45$ [Scherler et al., 2017], the generated φ-elevation
255 plots show a uniform trend (Figure 1c). We assumed the number of knickpoints to be 1 to 9 and
256 for each case, we performed 5000 realizations of the inversion with randomly selected positions
257 of knickpoints. For each model run, we modeled river φ-elevation plots via Equation (31) and
258 calculated the elevation misfit by Equation (32). We listed the elevation misfit as a function of
259 the number of assumed knickpoints and presented the non-dimensional uplift history that
260 corresponds to the minimum misfit value at two knickpoints (Figure 1d-e). The results of Figure
261 1c-e are nearly the same to those in Wang et al. [2022].

262 In this case, we fixed parameters, $a = 3/2$, $\omega_s = 0.25$, $\omega_b = 0.55$, $\tau_c = 45$ Pa, $k_e =$
263 4.3×10^{-12} m$^{2.5}$s^{2}kg$^{-1.5}$, $k_t = 1000$ m$^{-7/3}$s$^{-4/3}$kg, and $k_w = 15$ m$^{-0.65}$s$^{0.55}$ [Dibiase and
264 Whipple, 2011]. Next, we estimated the parameters, R_b and k, based on the monotonic, positive
265 non-linearity between erosion rates with channel steepness:

$$k_s = k_\Phi \cdot E^\Phi \ (33)$$

267 Ouimet et al. [2009] reported a data set of $E - k_s$ in the Dadu and adjacent river catchments. A
268 free fit to the data produced the exponent $\Phi = 0.4874$ (Figure 2). Assigning the k_s data of
269 Ouimet et al. [2009] into Equations (18 and 10), we calculated erosion rates and the statistic
270 scaling between the rates and steepness indices. The resulted parameters, Φ and k_Φ, vary a lot for
271 changes in R_b and k (Figure 3).
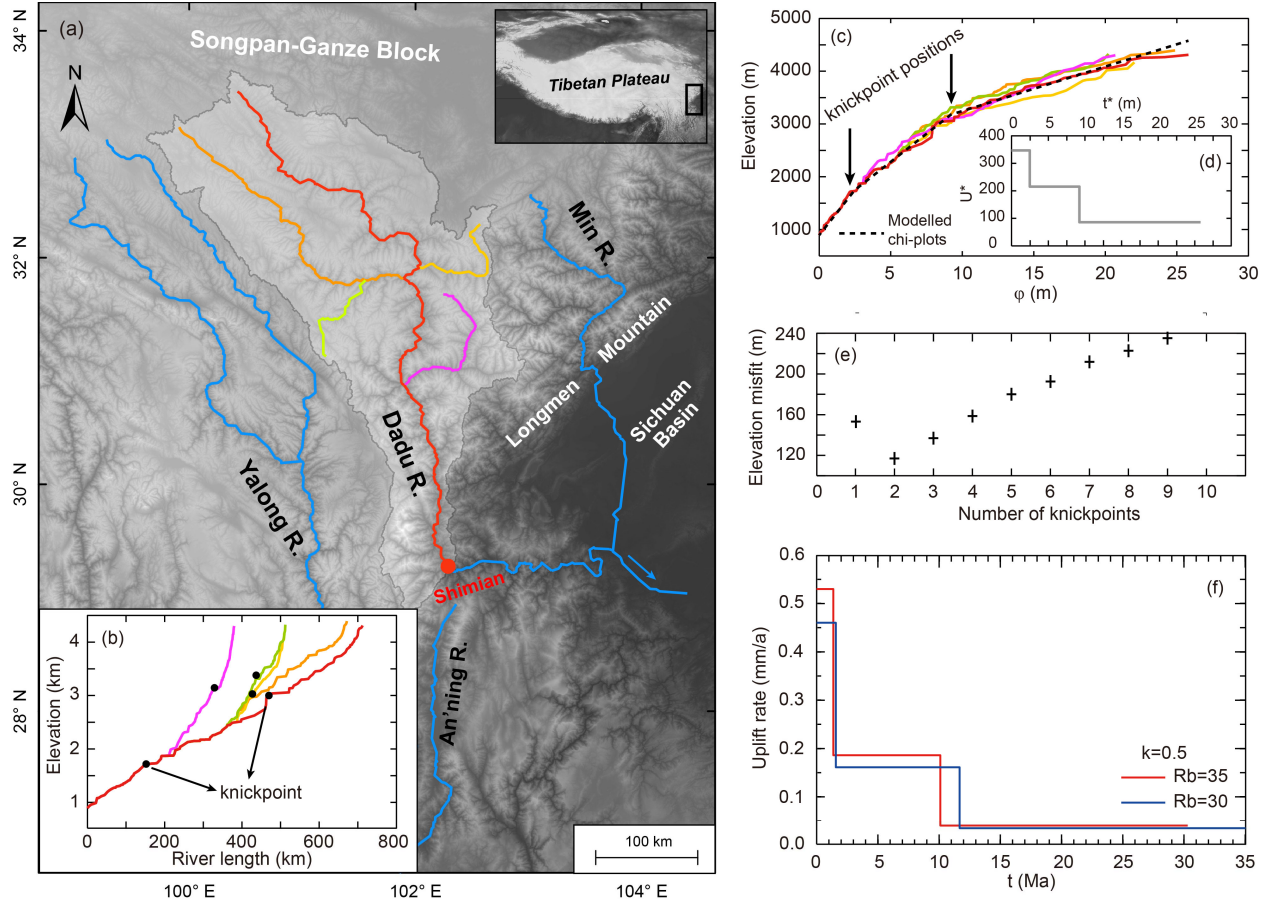
272

273

274 Figure 1. (a) Location of the Dadu River basin. The long, main trunks selected for inversion are in colors. (b)
275 The long profiles of the selected trunk channels, with prominent knickpoints labeled in black dots. (c) The
276 colored, solid lines are the φ-elevation plots of the main trunks and the black, dashed line is the best-fit inferred
277 φ-elevation plot with the history shown in (d). (d) The non-dimensional history of relative uplift rate with the
278 best-fit solution by using two knickpoints. (e) The elevation misfit as a function of the number of division
279 points, based on equation (32). (f) The inferred dimensional uplift history with the same runoff variability but
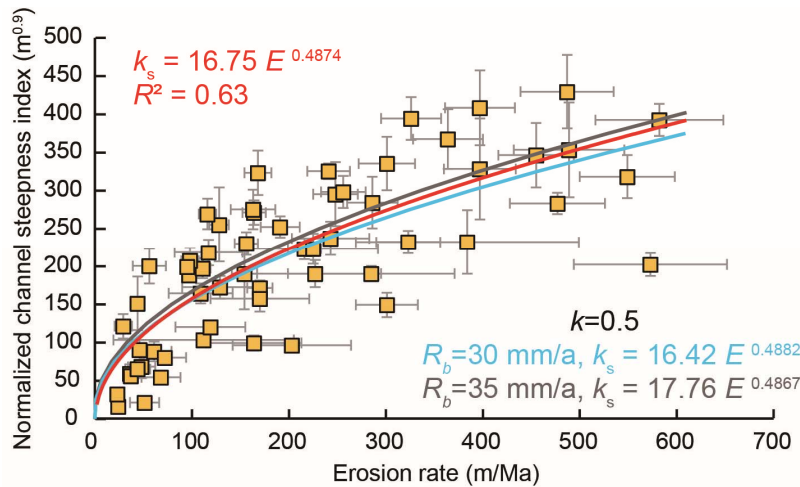280 different R_b values.

281

282

283 Figure 2. The non-linearity of the measured erosion rates and channel steepness. The data with error bars (1σ
284 uncertainty) are from Ouimet et al. [2009]. Red line indicates a free fit to the dataset. Gray and blue lines show
285 the best fit of Equation (10) through erosion rates, using the same runoff variability but different R_b values.

286

287 Figure 3a shows that, when $k \geq 1$ and R_b is no more than 2000 mm/a, the Φ is always
288 below 0.45. Although Φ has the potential to be over 0.45 for much higher runoff, the coefficient
289 k_Φ is getting close to zero (Figure 3b). Figure 3c and e indicates that, as long as $k \leq 0.4$, the Φ is
290 higher than 0.5. If $k \geq 0.6$, the high runoff $(R_b \geq 500)$ produces a Φ that is close to 0.48 but
291 $k_\Phi < 10$ (Figure 3e-f). When $k = 0.5$ and $30 \leq R_b \leq 35$, we obtained $\Phi \sim (0.4867, 0.4882)$
292 and $k_\Phi \sim (16.42, 17.76)$ (Figure 3g-h). This is consistent with the results of the free fit to the $E -$
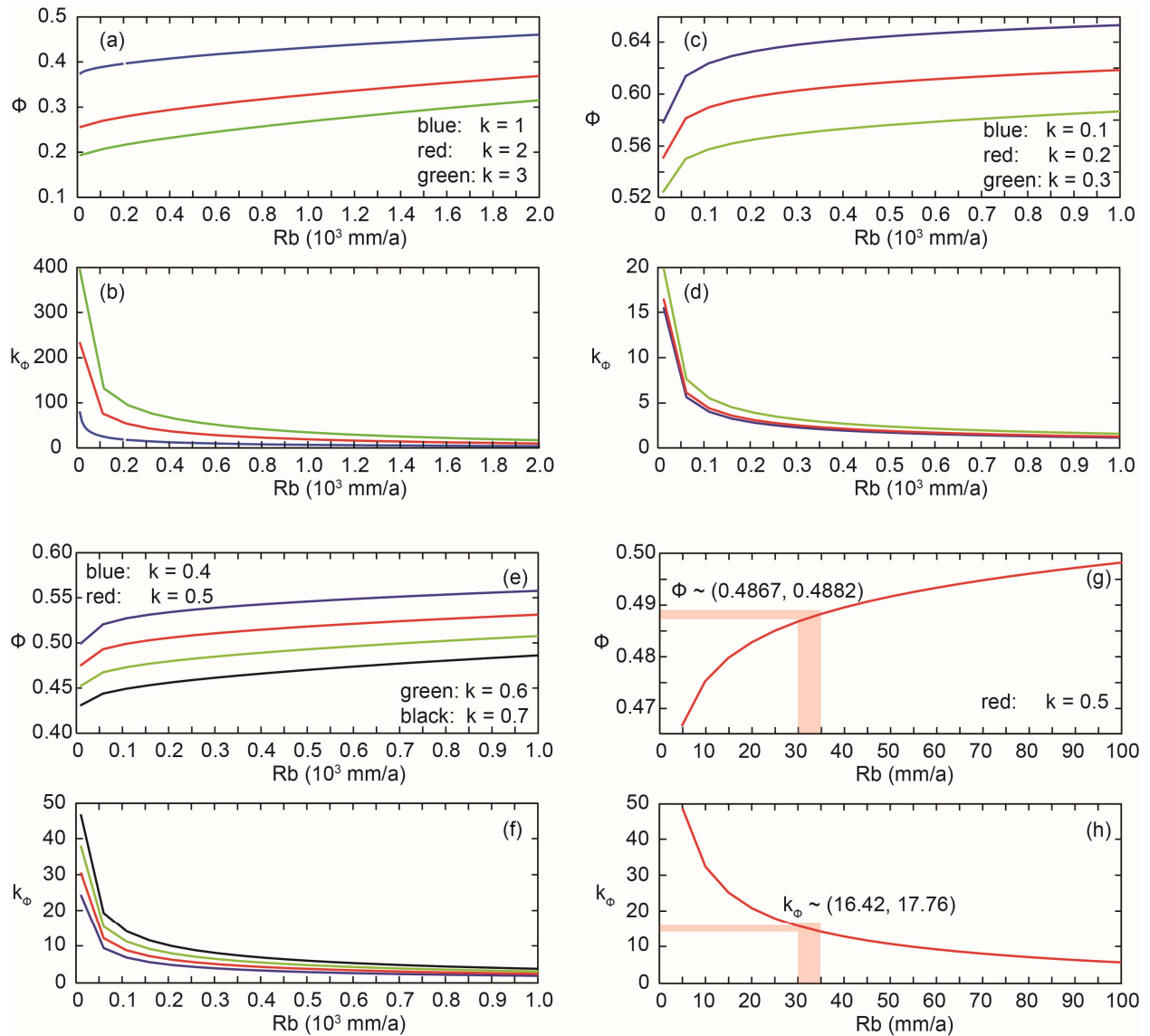293 k_s dataset (Figure 2).

294

296 Figure 3. The coefficient (k_Φ) and exponent (Φ) of the erosion rate – channel steepness scaling change as a
297 function runoff (R_b) and its variability (k).

298

299   Thus, we fixed $k = 0.5$ and used $R_b = 30$ and 35 to calculate the history of relative uplift
300   rates. Both the two histories nearly show the same trend with two-phase of increase in the uplift
301   rates since the Miocene, i.e. one is at 10-12 Ma (the rate increased from 0.05 to ~0.20 mm/a) and
302   another is at 1.5-2.0 Ma (from 0.20 to 0.45-0.55 mm/a). The inferred history is consistent with
303   the timing of the tectono-geometric events revealed by low temperature studies [e.g. Ouimet,
304   2007; Tian et al., 2015; Yang et al., 2019]. And, the history produces an average rate of relative
305   uplift to be about 0.25-0.30 mm/a (from 10-12 Ma to the present), which is similar to the incision
306   rates (derived from elevation transects of apatite fission track and Helium ages) along the trunk
307   channel of the Dadu River [Clark et al., 2005].

308

309   **6 Discussion**

310

311   **6.1 Limitation and assumption**

312   The analytic work we presented here was based on an essential assumption that erosion rate
313   depends on channel slope linearly, i.e. the slope exponent $n = 1$. This assumption relies on the
314   combination of a non-linear relation ($a = 3/2$ in Equation 2) between instantaneous incision rate
315   with shear stress and a Darcy-Weisbach relation ($\alpha = \beta = 2/3$ in Equation 3) between shear
316   stress with channel slope [Howard, 1994]. In the simple SPIM (Equation 1), the non-linearity in
317   the $E - k_s$ scaling is directly parameterized in the non-linear exponent n [Whipple and Tucker,
318   1999]. Although the non-linear n could cause complex fluvial dynamics [Royden and Perron,
319   2013], Wang et al. [2022] developed an inverse model to extract tectonic uplift history based on
320   the assumption of knickpoint preservation. Choosing the same trunk rivers as a case, both Wang
321   et al. [2022] and this study nearly inferred the same dimensional uplift rate histories. Thus,
322   applying a linear n in the stochastic-threshold incision model can also solve some inverse
323   problems relating to the non-linear dependence of channel steepness on river erosion rate.

324   Another limitation is that our model uses constant runoff and variability. In the case study,
325   we obtained runoff of 30-35 mm/a and variability parameter $k = 0.5$ to best match the observed
326    $E - k_s$ scaling. However, for the rivers southeast to the Dadu, the runoff recorded by modern
327   hydrological stations is more than 500 mm/a and $k > 3$ [Scherler et al., 2017]. That might be
328   because that those stations are mainly on large rivers, while the $E - k_s$ dataset are mostly from
329   small-scale tributary catchments of the Dadu River [Ouimet et al., 2009]. It means that the
330   climate parameters that was calibrated via the dataset of small catchments were extrapolated to
331   the inversion on the long, main trunks of the Dadu basin. The inferred history is well consistent
332   with the exhumation history along the trunk of the Dadu River [Clark et al., 2005], which might
333   indicate a consistence in the adjustment response of both trunk and tributary channels to the
334   changes in incision and/or uplift rates. It also implies that the $E - k_s$ scaling at 10^3-10^4 yr scale
335   can be extrapolated to a long time scale of $>10^6$ yr. Despite the global climate changes since 2-4
336   Ma [Zhang et al., 2001], both numerical and analytical models show that the high-frequency
337   oscillations are not expected to leave significant effects on the topography of bedrock fluvial
338   channels [Goren et al., 2016].

339

340 **6.2 Whether knickpoints can be preserved**

341   Our analytical solution and inverse method are both based on the premise of no knickpoint
342 merge. Here, we demonstrated that, under the linear stochastic-threshold incision model, all the
343 knickpoints can be well preserved. Taking the transformation of Equations (17, 27 and 28), we
344 can write:

345
$$\frac{\partial z}{\partial t} = \frac{\partial z}{\partial t^*} \cdot \frac{dt^*}{dt} = \frac{\partial z}{\partial t^*} \cdot A_0^{cm} \cdot K'(Q_c^*) \ (34)$$

346
$$\frac{\partial z}{\partial x} = \frac{\partial z}{\partial \varphi} \cdot \frac{d\varphi}{dx} = \frac{\partial z}{\partial \varphi} \cdot [\frac{A_0}{A(x\prime)}]^{cm} \ (35)$$

347 Substituting Equations (34-35) into (19):

348
$$\frac{\partial z}{\partial t^*} \cdot A_0^{cm} \cdot K'(Q_c^*) + K'(Q_c^*) \cdot A(x)^{cm} \cdot \frac{\partial z}{\partial \varphi} \cdot [\frac{A_0}{A(x)}]^{cm} = U(t) + E_c(Q_c^*) \ (36)$$

349   Our approach resolved knickpoint kinematics in a Lagrangian reference frame, which
350 implies that, along a channel segment between two adjacent knickpoints, K' should be a constant.
351 Thus, Equation (36) can be re-arranged as:

352
$$\frac{\partial z}{\partial t^*} + \frac{\partial z}{\partial \varphi} = \frac{U(t)+E_c}{A_0^{cm} \cdot K\prime} = U^*(t^*) \ (37)$$

353 One of the characteristic equations of Equation (37) is:

354
$$d\varphi/dt^* = 1 \ (38)$$

355 Thus, taking the transformation of Equations (17, 27 and 28), the transient signals (knickpoints)
356 migrates at the same velocity in the φ-elevation domain. Thus, our inverse scheme based on the
357 analytical solution to the linear STIM can deal with inverse problems relating to a nonlinear $E -$
358 k_s scaling, without the assumption of knickpoint preservation.

359   Notably, we do not mean that all the nonlinear $E - k_s$ cases can be resolved by the simple
360 stochastic-threshold model. Nevertheless, a combination of this approach and previous analytical
361 studies on $n \neq 1$ [e.g. Royden and Perron, 2013; Wang et al., 2022] could produce better
362 understandings on more complex fluvial dynamics. Besides, incorporating our analytical
363 procedures into forward and inverse tectonic – fluvial landscape evolution models [e.g. Fox et
364 al., 2015; Gallen and Fernández-Blanco, 2021; Steer et al. 2021] has the potential to significantly
365 expedite the model run speed and to make these models more efficient and accurate.

366

367 **7 Conclusion**

368   In this contribution, we presented analytical solutions to the simple stochastic-threshold
369 incision model equation. The solution to the steady-state equation of the model produces a φ-
370 elevation transformation to river long profile. Under the assumptions of a linear slope exponent
371 and the timely dependent uplift, we derived a closed-form analytical solution to the transient
372 state equation. This solution allows to relate the topography along fluvial channels to the history
373 of the relative uplift rate through time. Based on the analytical analysis, we developed a linear
374 inversion scheme to retrieve the tectonic uplift rate history from river long profiles. We applied
375 the inverse method to the Dadu River basin where channel steepness indices scale with
376 catchment erosion rates non-linearly. We inferred a history with two-stage increases in the

377 uplift/incision rates since the late Miocene, which is consistent with the exhumation history
378 recorded by low-temperature thermochronology. Our analytical procedures thus provide
379 powerful tools for understanding the transient behavior of bedrock channel evolution.

380

Acknowledgments

385

Open Research

387 The 90 m Shuttle Radar Topography Mission (SRTM) DEM (digital elevation model) data
388 can be freely downloaded at https://earthexplorer.usgs.gov/ for the analysis on fluvial topography
389 of the Dadu River basin. There is no codes sharing issues, as all the results can be reproduced by
390 solving the equations in the text. We declare no conflict of interest.

391

References

393 Berlin, M.M., and Anderson, R.S. (2007). Modeling of knickpoint retreat on the Roan Plateau, western
394 Colorado. J. Geophys. Res., 112, F03S06, doi:10.1029/2006JF000553.

395 Clark, M.K., House, M.A., Royden, L.H., Whipple, K.X., Burchfiel, B.C., Zhang, X., and Tang, W., (2005).
396 Late Cenozoic uplift of southeastern Tibet. Geology, 33(6): 525‑528. doi:
397 https://doi.org/10.1130/G21265.1

398 Clark, M.K., Schoenbohm, L.M., Royden, L.H., Whipple, K.X., Burchfiel, B.C., Zhang, X., Tang, W., Wang,
399 E., and Chen, L., (2004). Surface uplift, tectonics, and erosion of eastern Tibet from large-scale
400 drainage patterns. Tectonics 23, TC1006.

401 DiBiase, R. A., and K. X. Whipple (2011). The influence of erosion thresholds and runoff variability on the
402 relationships among topography, climate, and erosion rate, J. Geophys. Res., 116, F04036,
403 doi:10.1029/2011JF002095.

404 Fox, M., Bodin, T., and Shuster, D.L. (2015). Abrupt changes in the rate of Andean Plateau uplift from
405 reversible jump Markov Chain Monte Carlo inversion of river profiles. Geomorphology 238:1–14.

406 Gallen, S. F., and Fernández-Blanco, D. (2021). A new data-driven Bayesian inversion of fluvial topography
407 clarifies the tectonic history of the corinth rift and reveals a channel steepness threshold. J. Geophys.
408 Res. Earth, 126, e2020JF005651. https://doi.org/10.1029/2020JF005651.

409 Goren, L. (2016). A theoretical model for fluvial channel response time during time-dependent climatic and
410 tectonic forcing and its inverse applications, Geophys. Res. Lett., 43, 10,753‑10,763,
411 doi:10.1002/2016GL070451.

412 Goren, L., Fox, M., and Willett, S.D. (2014). Tectonics from fluvial topography using formal linear inversion:
413 theory and applications to the Inyo Mountains, California. J. Geophys. Res. Earth 119:1651–1681.

414 Goren, L., Fox, M., and Willett, S. D. (2021). Linear Inversion of Fluvial Long Profiles to Infer Tectonic
415 Uplift Histories, Reference Module in Earth Systems and Environmental Sciences, Elsevier, ISBN
416 9780124095489, https://doi.org/10.1016/B978-0-12-818234-5.00075-4.

417 Harel, M.-A., Mudd, S.M., and Attal, M. (2016). Global analysis of the stream power law parameters based on
418   worldwide 10Be denudation rates. Geomorphology 268, 184-196.
419   doi:10.1016/j.geomorph.2016.05.035

420 Harkins, N., Kirby, E., Heimsath, A., Robinson, R., and Reiser, U. (2007). Transient fluvial incision in the
421   headwaters of the Yellow River, northeastern Tibet, China. J. Geophys. Res. Earth 112: F03S04.

422 Johnson, J.P., and Whipple, K.X., (2007). Feedbacks between erosion and sediment transport in experimental
423   bedrock channels: earth Surface Processes and Landforms. Earth Surf. Process. Landforms 32, 1048-
424   1062.

425 Hilley, G.E., Porder, S., Aron, F., Baden, C.W., Johnstone, S.A., Liu, F., Sare, R., Steelquist, A., and Young,
426   H.H., (2019). Earth's topographic relief potentially limited by an upper bound on channel steepness.
427   Nat. Geosci. 12: 828–832.

428 Howard, A. D. (1994). A detachment limited model of drainage-basin evolution, Water Resour. Res., 30(7),
429   2261‐2285, doi:10.1029/94WR00757.

430 Howard, A.D., and Kerby, G. (1983). Channel changes in badlands. Geol. Soc. Am. Bull. 94, 739-752.

431 Kirby, E., and Whipple, K.X. (2012). Expression of active tectonics in erosional landscapes. J. Struct. Geol.
432   44:54–75. http://dx.doi.org/10.1016/j.jsg.2012.07.009

433 Lague, D. (2014). The stream power river incision model: evidence, theory and beyond. Earth Surf. Process.
434   Landf. 39, 38–61.

435 Lague, D., Hovius, N. and Davy, P. (2005). Discharge, discharge variability, and the bedrock channel profile,
436   J. Geophys. Res., 110, F04006, doi:10.1029/2004JF000259.

437 Montgomery, D. R., and K. B. Gran (2001). Downstream variations in the width of bedrock channels, Water
438   Resour. Res., 37(6), 1841‐1846, doi:10.1029/2000WR900393.

439 Ouimet, W.B., Whipple, K.X., and Granger, D.E. (2009). Beyond threshold hillslopes: channel adjustment to
440   base-level fall in tectonically active mountain ranges. Geology 37(7), 579–582.
441   http://dx.doi.org/10.1130/G30013A.1.

442 Perron, J.T., and Royden, L. (2013). An integral approach to Bedrock River profile analysis. Earth Surf.
443   Process. Landf. 38:570–576. http://dx.doi.org/10.1002/esp.3302.

444 Pritchard, D., Roberts, G.G., White, N.J., and Richardson, C.N. (2009). Uplift histories from river profiles.
445   Geophys. Res. Lett., 36, L24301. doi:10.1029/2009GL040928

446 Refice, A., Giachetta, E., and Capolongo, D. (2012). Signum: a MATLAB, tin-based landscape evolution
447   model. Computers and Geosciences 45(0): 293‐303.

448 Royden, L., and Perron, J.T. (2013). Solutions of the stream power equation and application to the evolution of
449   river longitudinal profiles. J. Geophys. Res. Earth 118 (2):497–518.
450   http://dx.doi.org/10.1002/jgrf.20031.

451 Rudge, J.F., Roberts, G.G., White, N.J., and Richardson, C.N. (2015). Uplift histories of Africa and Australia
452   from linear inverse modeling of drainage inventories. J. Geophys. Res. Earth 120, 894–914.

453 Scherler, D., DiBiase, R.A., Fisher, G.B., and Avouac, J.-P. (2017). Testing monsoonal controls on bedrock
454   river incision in the Himalaya and Eastern Tibet with a stochastic-threshold stream power model, J.
455   Geophys. Res. Earth Surf., 122, 1389‐1429, doi:10.1002/2016JF004011.

456 Snyder, N.P., Whipple, K.X., Tucker, G.E., and Merritts, D.J., (2003). Importance of a stochastic distribution
457   of floods and erosion thresholds in the bedrock river incision problem. J. Geophys. Res. 108, 2117.

458 Steer, P. (2021). Short communication: Analytical models for 2D landscape evolution. Earth Surf. Dynam.,
459   9(5), 1239-1250.

Tian, Y., Kohn, B.P., Hu, S., and Gleadow, A.J.W., (2015). Synchronous fluvial response to surface uplift in the eastern Tibetan Plateau: Implications for crustal dynamics, Geophys. Res. Lett., 42, 29‑35, https://doi.org/10.1002/2014GL062383.

Tucker, G. E. (2004). Drainage basin sensitivity to tectonic and climatic forcing: Implications of a stochastic model for the role of entrainment and erosion thresholds, Earth Surf. Processes Landforms, 29(2), 185‑205, doi:10.1002/esp.1020.

Tucker, G., Lancaster, S., Gasparini, N., and Bras, R. (2001). The channelhillslope integrated landscape development model (child). In Landscape Erosion and Evolution Modeling, Harmon RS, Doe WW III (eds). Springer: New York; 349‑388.

Wang, Y., Goren, L., Zheng, D., and Zhang, H., (2022). Short communication: Forward and inverse analytic models relating river long profile to tectonic uplift history, assuming a nonlinear slope‑erosion dependency, Earth Surf. Dynam., 10, 833‑849, https://doi.org/10.5194/esurf-10-833-2022.

Wang, Y., Liu, C., Zheng, D., Zhang, H., Yu, J., Pang, J., Li, C., and Hao, Y., (2021). Multistage exhumation in the catchment of the Anninghe River in the SE Tibetan Plateau: Insights from both detrital thermochronology and topographic analysis, Geophys. Res. Lett., 48, e2021GL092587, https://doi.org/10.1029/2021GL092587.

Whipple, K. X. (2009). The influence of climate on the tectonic evolution of mountain belts, Nat. Geosci., 2(10), 730, doi:10.1038/ngeo638.

Whipple, K.X., and Tucker, G.E. (1999). Dynamics of the stream power river incision model: Implications for height limits of mountain ranges, landscape response timescales and research needs, J. Geophys. Res., 104, 17,661–17,674.

Whipple, K.X., and Tucker, G.E. (2002). Implications of sediment-flux-dependent river incision models for landscape evolution. Journal of Geophysical Research, Solid Earth 107(B2). https://doi.org/10.1029/2000JB000044.

Yang, R., Suhail, H.A., Gourbet, L., Willett, S.D., Fellin, M.G., Lin, X., Gong, J.F., Wei, X.C., Maden, C., Jiao, R.H., and Chen, H.L., (2019). Early Pleistocene drainage pattern changes in Eastern Tibet: Constraints from provenance analysis, thermochronometry, and numerical modeling, Earth Planet. Sc. Lett., 531, 115955, https://doi.org/10.1016/j.epsl.2019.115955.

Zhang, H., E. Kirby, J. Pitlick, R. S. Anderson, and P. Zhang (2017). Characterizing the transient geomorphic response to base-level fall in the northeastern Tibetan Plateau, J. Geophys. Res. Earth Surf., 122, doi:10.1002/2015JF003715.

Zhang, P., Molnar, P., and Downs, W.R., (2001). Increased sedimentation rates and grain sizes 2‑4 Myr ago due to the influence of climate change on erosion rates. Nature, 410, 891‑897.